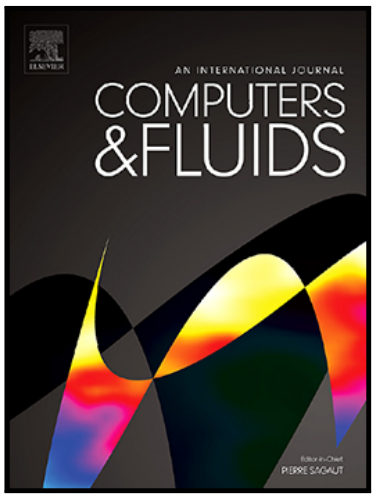

Numerical study of chemically reacting flow in a shock tube using a high-order point-implicit scheme

S. Chen, Q. Sun, I. Klioutchnikov, H. Olivier

PII: S0045-7930(18)30712-6
DOI: https://doi.org/10.1016/j.compfluid.2019.02.019
Reference: CAF 4133

To appear in: *Computers and Fluids*

Received date: 11 October 2018
Revised date: 22 January 2019
Accepted date: 24 February 2019

Please cite this article as: S. Chen, Q. Sun, I. Klioutchnikov, H. Olivier, Numerical study of chemically reacting flow in a shock tube using a high-order point-implicit scheme, *Computers and Fluids* (2019), doi: https://doi.org/10.1016/j.compfluid.2019.02.019

Highlights

- An integrated numerical methodology is developed and validated for reacting flow
- The unsteady shock wave/boundary-layer interaction is clearly captured and analyzed
- As Mach number increases, the vortex breaks up and chemical nonequilibrium arises
- The contribution of real gas effects is shown to be significant at Mach number 3.15

Numerical study of chemically reacting flow in a shock tube using a high-order point-implicit scheme

S. Chen[a,b], Q. Sun[c,d], I. Klioutchnikov[e], H. Olivier[e]

[a] *Department of Mechanics and Aerospace Engineering, Southern University of Science and Technology, Shenzhen 518055, People's Republic of China*
[b] *School of Power and Mechanical Engineering, Wuhan University, Wuhan 430072, People's Republic of China*
[c] *State Key Laboratory of High Temperature Gas Dynamics, Institute of Mechanics, Chinese Academy of Sciences, Beijing 100190, People's Republic of China*
[d] *School of Engineering Science, University of Chinese Academy of Sciences, Beijing 100049, People's Republic of China*
[e] *Shock Wave Laboratory, RWTH Aachen University, 52056 Aachen, Germany*

Abstract

The shock wave/boundary-layer interaction of chemically reacting flow in a shock tube is studied using a high-order point-implicit solver. The solver employs a high-resolution weighted essentially non-oscillatory (WENO) scheme to capture the complex shock structures, together with a point-implicit method to overcome the stiffness of the chemical production term in the multicomponent Navier-Stokes equations. The numerical code is carefully validated with three benchmark tests, which demonstrates the robustness and good performance of the combined numerical methods. The unsteady interaction process between the shock wave and boundary layer in a two-dimensional shock tube is clearly captured with detailed flow patterns in the simulation. Simulation results show that regular vortex arrangements appear in the flow field for the case of Mach number 2.37, while for the case of Mach number 3.15, the vortex structures break up and chemical nonequilibrium effects become apparent. The influence of real gas effects on shock wave/boundary-layer interaction is further identified on the temperature field and triple point trajectory.

Keywords: shock wave/boundary-layer interactions, real gas effects, chemical nonequilibrium, high-order scheme

1. Introduction

The shock tube is an important facility for the study of high temperature gas reactions and many others [1]. The region behind the reflected shock wave near the end wall provides theoretically uniform, stationary and high enthalpy gas which is ideally suited for the investigation of chemical kinetics in reactive gas mixtures. However, in a real shock tube the non-uniformities are inevitable introduced into the flow due to many factors, such as non-ideal rapture of the diaphragm, interface instability, and shock wave/boundary-layer interactions (SBLIs). The SBLIs can change flow properties significantly in the shock tube, leading to the so called "driver gas contamination" problem [2], which has attracted intensive studies [3, 4, 5, 6, 7, 8]. In recent years, SBLIs receive continuous attention [9, 10, 11, 12, 13], because they are not only fundamental in fluid dynamics that deserve further investigations, but also critical to a number of applications such as design in transonic airfoils, supersonic/hypersonic inlets, scramjet combustor and so on.

When an incident shock wave reflects at the end wall of a shock tube and interacts with the boundary layer, the following process is complex and unsteady. Investigation on this problem was pioneered by Mark [3] in 1958 who proposed a theoretical model to analyze the interaction between the reflected shock wave and boundary layer, or in other words, the shock bifurcation process. Mark's model was later improved and extended by many researchers [4, 5]. The theoretical model is able to predict very basic bifurcation characteristics, such as the shock angle of the bifurcated foot and velocity of the reflected shock. However, it cannot reveal the detailed flow information due to the complexity of the problem.

Numerical approaches were then applied to study the problem in 1990s. Weber *et al.* [6] performed an early numerical study of two dimensional viscous flow in a shock tube using a Flux-Corrected Transport (FCT) algorithm. They investigated the effects of Mach number and wall temperature on the shock bifurcation process, and found that increasing the Mach number of the incident shock leads to stronger reflected SBLIs, which cause multiple, weak shocks to appear beneath the λ-shock structure. However, the FCT algorithm they used only retains the second order accuracy thus the fine vortex was not depicted. In 2003, Sjogreen and Yee [14] employed several high-order schemes and found that extreme grid refinement was required to resolve detailed flow structures. With the rapid growth of the computational capability, Daru and Tenaud [15] later showed the converged results for the

Reynolds number up to 1000. The high resolution flow field presented in Daru and Tenaud's work indicated a very complex unsteady interaction taking place between the reflected shock wave and the incident boundary layer. They concluded that calculation of such a complex flow requires numerical schemes which are both robust and accurate.

While the aforementioned numerical studies are focused on the viscous flow without chemical reactions, the simulation of chemically reactive flow is much more challenging. Chemical reactions not only increase the number of equations to be solved but also make the equation system "stiff" due to the chemical source terms. To simply the problem, Chen *et al.* [10] assumed chemical equilibrium for the numerical study of high-speed flow in an air-He shock tube, and adopted curve-fitting approximation for equilibrium air. The driver gas contamination and the development of SBLIs are presented with high quality flow visualization. They found that the real gas effects have significant influence on the temperature behind the reflected shock. Recently, Ferrer *et al.* [16] developed a Navier-Stokes solver for reactive flow by employing a 3-order Runge-Kutta time integration scheme and a 7-order WENO scheme. The solver employed the EGLIB library [17, 18] to evaluate the transport properties for gas mixture, and showed a good performance in dealing with chemical nonequilibrium flows. There are also numerical investigations of the reflected SBLIs problem using high-order schemes (e.g. Ref. [11]). However, sufficient grid convergence proof and detailed analysis with respect to the real gas effects are barely seen in the relevant studies.

Our primary objective is to investigate the real gas effects on the complex shock wave and boundary layer interactions for air flow in a shock tube. For this purpose, we firstly develop a Navier-Stokes solver with parallel capability. The solver uses a fifth-order WENO scheme to calculate the inviscid fluxes, a sixth-order central difference scheme to evaluate the viscous flux, and a point-implicit method to conduct time integration. Some preliminary results have been reported in a conference paper [19]. In the present study, the solver is further validated using several typical test cases. Then, it is applied to study a two-dimensional shock tube flow with real gas effects, which means that the vibrational excitation and chemical reactions are taken into account [20, 21]. After careful grid study, the detailed SBLIs process and the influence of real gas effects are analyzed and discussed.

2. Numerical procedures

2.1. Governing equations

The Navier-Stokes equations that govern compressible multicomponent flows are written in dimensionless form as

$$\frac{\partial \rho_s}{\partial t} + \frac{\partial \rho_s u_j}{\partial x_j} = -\frac{1}{\mathbf{Re}_r \mathbf{Sc}} \frac{\partial J_{j,s}}{\partial x_j} + \dot{\omega}_s, \tag{1}$$

$$\frac{\partial \rho u_i}{\partial t} + \frac{\partial \rho u_i u_j}{\partial x_j} = -\frac{1}{\gamma_r \mathbf{M}_r^2} \frac{\partial p}{\partial x_i} + \frac{1}{\mathbf{Re}_r} \frac{\partial \tau_{ij}}{\partial x_j}, \tag{2}$$

$$\frac{\partial \rho e_t}{\partial t} + \frac{\partial (\rho e_t + p) u_j}{\partial x_j} = \frac{\partial u_i \tau_{ij}}{\partial x_j} + \frac{1}{(\gamma_r - 1)\mathbf{Re}_r \mathbf{Pr} \mathbf{M}_r^2} \frac{\partial q_j}{\partial x_j}, \tag{3}$$

where ρ and e_t are the density and total energy per unit mass, respectively. u_i is the velocity component in i direction. $Y_s = \rho_s/\rho$ is the species mass fraction of the sth species (s=1,2,...,ns), and $\dot{\omega}_s$ is the chemical source term. τ_{ij} is the Newtonian shear stress tensor. q_j and $J_{j,s}$ are the j-component heat flux and species diffusive flux, respectively.

The parameters are non-dimensionlized using the denotation system in [22]. Namely, the subscript r denotes a reference value, an asterisk represents dimensional variables, and a dimensionless parameter is defined as the ratio of dimensional variable to its reference value, e.g. $p = p^*/p_r^*$. In particular, the Reynolds number $\mathbf{Re}_r = \rho_r^* u_r^* L_r^*/\mu_r^*$ and the Mach number $\mathbf{M}_r = u_r^*/\sqrt{\gamma_r R_r^* T_r^*}$. Other parameters, like $\dot{\omega}_s$, τ_{ij}, q_j and $J_{j,s}$ will be specified later.

The Schmidt number and Prandtl number are treated as constants with $\mathbf{Sc} = 0.5$, $\mathbf{Pr} = 0.73$. The assumption of a constant $\mathbf{Pr}$ is well satisfied for most hot air flows as stated in [23]. Many authors assume a constant Lewis number for study of combustion (e.g., [24, 25]), which is equivalent to set a constant Schmidt number $\mathbf{Sc}$.

For multicomponent, chemically reacting gas flows where intermolecular forces are neglected, the equation of state for perfect gas still holds [26]

$$p = \rho R T, \tag{4}$$

where $R = R^*/R_r^*$ is the dimensionless gas constant of the mixture, which depends on the composition of the gas mixture. As for perfect gas R=1, and $p = \rho T$.

The total energy per unit mass is given by

$$e_t^* = \frac{1}{2}u_i^{*2} + \sum_{s=1}^{ns} Y_s(h_s^* - R_s^* T^*), \tag{5}$$

where R_s^* is the gas constant of species s. The enthalpy of species s can be expressed as a polynomial form of the temperature $h_s^* = h_s(T^*)$, and the corresponding coefficients are evaluated using NASA Glenn's library of thermodynamic data published in [27]. When the temperature is to be determined from the total energy, the *Newton-Raphson method* is employed for the iteration. It should be mentioned that the data for species properties take the vibrational excitation into account by assuming local thermal equilibrium. Thus, only chemical nonequilibrium is considered in the present study.

The transport properties of gas mixture are rather complex if the kinetic theory is strictly followed [17]. Ern and Giovangigli [17, 18] developed iterative methods to obtain an approximate solution of the transport coefficients. Ferrer *et al.* [16] found that the results achieved with a detailed transport description are actually very close to those obtained using the simplified transport expressions of Ern and Giovangigli (ignores the bulk viscosity as well as Soret and Dufour effects). Therefore, the simplified approach of transport coefficient evaluation is adopted in this paper in order to reduce the computational cost. The shear stress tensor is given in terms of the dynamic viscosity μ as

$$\tau_{ij} = \mu\left(\frac{\partial u_j}{\partial x_i} + \frac{\partial u_j}{\partial x_i} - \frac{2}{3}\delta_{ij}\frac{\partial u_k}{\partial x_k}\right), \tag{6}$$

where the mixture viscosity is estimated using Wilke's formula [28], and the viscosities of individual species are obtained from standard kinetic theory [26].

The dimensionless diffusive flux of species s in j direction is calculated based on Fick's law

$$J_{j,s} = -\rho D_s \frac{\partial Y_s}{\partial x_j}, \tag{7}$$

where D_s is the effective binary diffusion coefficient for each species. From the above expression a diffusion velocity $V_{j,s} = -(D_s/Y_s)\nabla Y_s$ can be deduced. To ensure that the sum of diffusion fluxes is zero, D_s is replaced by a single binary coefficient D. As the Schmidt number is assumed constant $\mathbf{Sc} =$

$\mu_r^*/(\rho_r^* D_r^*) = \mu^*/(\rho^* D^*)$, we have

$$D = \frac{\mu}{\rho}. \tag{8}$$

The heat flux is expressed as

$$q_j = \lambda \frac{\partial T}{\partial x_j} + \sum_{s=1}^{ns} J_{j,s} h_s, \tag{9}$$

where the heat conduction coefficient λ is obtained using the constant Prandtl number assumption: $\mathbf{Pr} = \mu_r^* c_{p,r}^* / \lambda_r^* = \mu^* c_p^* / \lambda^*$. Thus, the dimensionless heat conduction coefficient is

$$\lambda = \mu c_p, \tag{10}$$

where $c_p = c_v \gamma / \gamma_r$ (for perfect gas c_p=1, then $\lambda = \mu$).

To evaluate the chemical reaction source, the general finite rate reaction equation is written as

$$\sum_{s=1}^{N} v_{s,r}^{'} X_s \leftrightharpoons \sum_{s=1}^{N} v_{s,r}^{"} X_s, \quad (r = 1, 2, \ldots, nr) \tag{11}$$

where "nr" is the number of reactions and the chemical source term is

$$\dot{\omega}_s^* = M_s^* \sum_{ir=1}^{nr} (v_{s,r}^{"} - v_{s,r}^{'}) \left[k_{f,ir}^* \prod_{s=1}^{N} (\frac{\rho_s^*}{M_s^*})^{v_{s,r}^{'}} - k_{b,ir}^* \prod_{s=1}^{N} (\frac{\rho_s^*}{M_s^*})^{v_{s,r}^{"}} \right]. \tag{12}$$

The classical Arrhenius law $k^* = A^*(T^*)^\alpha exp(-\Theta^*/T^*)$ is used to model the forward reaction rate coefficient $k_{f,ir}^*$, and the Θ^* is the activation energy of chemical reaction. The backward reaction rate coefficient, $k_{b,ir}^*$, is calculated either using an Arrhenius form, or via the equilibrium constant $k_{b,ir}^* = k_{f,ir}^* / K_{eq}^*$, depending on the specific kinetic model. Two chemical kinetic models are used in the present simulation of nonequilibrium dissociation of air, one is Dunn and Kang's model[29], the other is Park's model[30]. The chemical source term is non-dimensionalized by

$$\dot{\omega}_s = \frac{\dot{\omega}_s^*}{\rho_r^* u_r^* / L_r^*}. \tag{13}$$

2.2. Space discretization

The kernel of the present solver is based on a finite difference scheme with the inviscid fluxes being approximated by the fifth-order WENO scheme of Jiang and Shu [31]. The basic formulations are briefly described below.

Firstly, the approximation of inviscid fluxes is conducted on a five points stencil

$$\begin{aligned} \left.\frac{\partial f}{\partial \xi}\right|_i &= \frac{f_{i+\frac{1}{2}} - f_{i-\frac{1}{2}}}{\triangle \xi}, \\ f_{i+\frac{1}{2}} &= \hat{\omega}_0 P_0 + \hat{\omega}_1 P_1 + \hat{\omega}_2 P_2, \end{aligned} \tag{14}$$

where P_0, P_1 and P_2 are the sub-stencils that contains three grid points. $\hat{\omega}_m$ is the normalized weight coefficient and ω_m is expressed as

$$\omega_m = \frac{b_m^r}{(\varepsilon + IS_m)^p}. \tag{15}$$

The parameter ε is a small value to avoid a total value of zero in the denominator. In the present study, $\varepsilon = 10^{-13}$ is used for all the simulations. b_m^r are the optimal weight coefficients that give fifth order approximation of smooth functions. IS_m are the smoothness indicators and $p = 2$ is chosen for all computations.

The reconstructed flux can be written in the the form of a central and upwind part [32],

$$f_{i+\frac{1}{2}} = \underbrace{\frac{1}{12}[-f_{i-1} + 7f_i + 7f_{i+1} - f_{i+2}]}_{\textbf{central}} - \underbrace{\varphi_N(\triangle f_{i-\frac{3}{2}}, \triangle f_{i-\frac{1}{2}}, \triangle f_{i+\frac{1}{2}}, \triangle f_{i+\frac{3}{2}})}_{\textbf{upwind}}, \tag{16}$$

with the weight operator

$$\varphi_N(a, b, c, d) = \frac{1}{3}\omega_0(a - 2b + c) + \frac{1}{6}(\omega_2 - \frac{1}{2})(b - 2c + d). \tag{17}$$

Together with the Lax-Friedrichs Flux-Vector Splitting scheme, the fifth-order WENO numerical flux is finally expressed as

$$\begin{aligned} \hat{F}_{i+\frac{1}{2}} &= \frac{1}{12}[-F_{i-1} + 7F_i + 7F_{i+1} - F_{i+2}] \\ &+ \sum_{s=1}^{m} [-\varphi_N(\triangle F^{s+}_{i-\frac{3}{2}}, \triangle F^{s+}_{i-\frac{1}{2}}, \triangle F^{s+}_{i+\frac{1}{2}}, \triangle F^{s+}_{i+\frac{3}{2}}) \\ &+ \varphi_N(\triangle F^{s-}_{i+\frac{5}{2}}, \triangle F^{s-}_{i+\frac{3}{2}}, \triangle F^{s-}_{i+\frac{1}{2}}, \triangle F^{s-}_{i-\frac{1}{2}}]\mathbf{R}_{s,i+\frac{1}{2}}, \end{aligned} \tag{18}$$

with

$$\begin{aligned}
&\triangle F^{s\pm}_{i+\frac{1}{2}} = \mathbf{L}_{s,i+\frac{1}{2}} \triangle F^{\pm}_{i+\frac{1}{2}}, \qquad (s = 1, 2, \ldots, m) \\
&\triangle F^{\pm}_{i+\frac{1}{2}} = F^{\pm}_{i+1} - F^{\pm}_{i}, \\
&F^{\pm}_{i} = \frac{1}{2}(F_i \pm \lambda^{max} U_i),
\end{aligned} \tag{19}$$

where m is the number of components in the solution vector U. The λ_i^{max} is the maximum eigenvalue on the stencil cells. In the calculation of left and right eigenvectors $\mathbf{L}_{s,i+\frac{1}{2}}$ and $\mathbf{R}_{s,i+\frac{1}{2}}$, the flow variables $(\rho, u, p, ...)$ are averaged between cell i and $i+1$. The detailed expression of eigenvectors are listed in Appendix A.

The viscous fluxes are discretized by means of a sixth-order accurate central scheme, which is sufficient to maintain the overall high-order properties of the numerical scheme.

2.3. The point-implicit method

In order to incorporate the advantages of implicit integration with respect to the source term of chemical reaction into an explicit method, it is common to treat the source term in a point-implicit manner [33, 34]. Take the one-dimensional case as example, the governing equation is expressed as follows [34]

$$\frac{\partial \mathbf{U}}{\partial t} + \frac{\partial \mathbf{F}}{\partial x} = \theta \mathbf{S}^{n+1} + (1-\theta)\mathbf{S}^{n}, \tag{20}$$

where θ is a introduced variable that changes between 0 to 1. In view of the above expression, we can write the conventional three stage Runge-Kutta integration as

$$\begin{aligned}
\mathbf{U}^{A} &= \mathbf{U}^{n} + \triangle t \left[-\frac{\partial \mathbf{F}(\mathbf{U}^{n})}{\partial x} + \theta \mathbf{S}^{A} + (1-\theta)\mathbf{S}^{n} \right], \\
\mathbf{U}^{B} &= \frac{3}{4}\mathbf{U}^{n} + \frac{1}{4}\mathbf{U}^{A} + \frac{1}{4}\triangle t \left[-\frac{\partial \mathbf{F}(\mathbf{U}^{A})}{\partial x} + \theta \mathbf{S}^{B} + (1-\theta)\mathbf{S}^{A} \right], \\
\mathbf{U}^{n+1} &= \frac{1}{3}\mathbf{U}^{n} + \frac{2}{3}\mathbf{U}^{B} + \frac{2}{3}\triangle t \left[-\frac{\partial \mathbf{F}(\mathbf{U}^{B})}{\partial x} + \theta \mathbf{S}^{n+1} + (1-\theta)\mathbf{S}^{B} \right].
\end{aligned} \tag{21}$$

in which the $\mathbf{S}^A$, $\mathbf{S}^B$ and $\mathbf{S}^{n+1}$ are approximated for each increment of $\mathbf{U}$ using first order Taylor expansion, i.e., $\mathbf{S}^B \approx \mathbf{S}^A + \frac{\partial \mathbf{S}}{\partial \mathbf{U}}(\mathbf{U}^B - \mathbf{U}^A)$. Thus, the

above equation can be rewritten as

$$\begin{aligned}
\left[\mathbf{I}-\theta\triangle t\frac{\partial \mathbf{S}}{\partial \mathbf{U}}\right](\mathbf{U}^A-\mathbf{U}^n)&=\triangle t\left[-\frac{\partial \mathbf{F}(\mathbf{U}^n)}{\partial x}+\mathbf{S}^n\right],\\
\left[\mathbf{I}-\frac{1}{4}\theta\triangle t\frac{\partial \mathbf{S}}{\partial \mathbf{U}}\right](\mathbf{U}^B-\mathbf{U}^A)&=\frac{3}{4}(\mathbf{U}^n-\mathbf{U}^A)+\frac{1}{4}\triangle t\left[-\frac{\partial \mathbf{F}(\mathbf{U}^A)}{\partial x}+\mathbf{S}^A\right],\\
\left[\mathbf{I}-\frac{2}{3}\theta\triangle t\frac{\partial \mathbf{S}}{\partial \mathbf{U}}\right](\mathbf{U}^{n+1}-\mathbf{U}^B)&=\frac{1}{3}(\mathbf{U}^n-\mathbf{U}^B)+\frac{2}{3}\triangle t\left[-\frac{\partial \mathbf{F}(\mathbf{U}^B)}{\partial x}+\mathbf{S}^B\right].
\end{aligned}\tag{22}$$

where $\mathbf{I}$ is the unit matrix. Therefore, the problem is transformed into solving the classical matrix equation

$$\mathbf{AX}=\mathbf{B},\tag{23}$$

at each Runge-Kutta step. Here $\mathbf{X}$ represents $\triangle\mathbf{U}$, $\mathbf{A}$ represents the coefficient matrix, and $\mathbf{B}$ represents the right-hand side terms. *Gaussian elimination with pivoting algorithm* is employed to solve the equation. It should be noted that if θ equals to 0, then the system reduce to the explicit Runge-Kutta integration. In the present study, θ is set to 1, which corresponds to the so called point-implicit method. The source term Jacobi matrix of $\partial\mathbf{S}/\partial\mathbf{U}$ that is involved in the procedure is listed in Appendix B.

3. Benchmark tests

Based on the above described numerical procedure, a CFD code named SCARF was first developed by the present authors during the collaborative research in the Shock Wave Laboratory (SWL) of RWTH Aachen University. The subroutine for the WENO scheme is adopted from a WENO5 code that has been used for the study of non-reacting flows in SWL [32, 35]. In this section, three typical benchmark tests were chosen to evaluate the performance of the code. The details are described in the following sub-sections.

3.1. Propagation of an acoustic wave

The first test case considered is an acoustic wave travelling across a periodic domain of length $L_{x_1}=5$ mm in a pure oxidizer mixture, which was previously studied by Vicquelin *et al.* [24] and re-examined recently by Ferrer *et al.* [16]. The aim is to verify the performance of the WENO scheme coupled with multicomponent diffusive terms. The composition of the oxidizer

mixture can be found in [24] or [16], while the initial conditions are given by

$$u_1 = 0.01\exp\left(-\frac{(x_1 - x_{1,0})^2}{d^2}\right), \qquad (24)$$
$$P = 1 + \gamma_0 u_1, \quad \rho = 1 + u_1,$$

where $d = 0.1$, $x_{1,0} = 0.5$, both non-dimensionlized by L_{x_1}. The initial specific heat ratio γ_0 is obtained by the sound speed a_0^*. The reference parameters are: $\rho_0^* = 0.24$ kg/m^3, a_0^* =734.6 m/s and $P_0^* = 1$ atm. The computational domain is discretized with 200 grid points and periodic conditions are applied at the boundaries. The CFL number is set to 0.5. The evolution of pressure and temperature at $x_1^* = 0$ are plotted in Fig. 1.

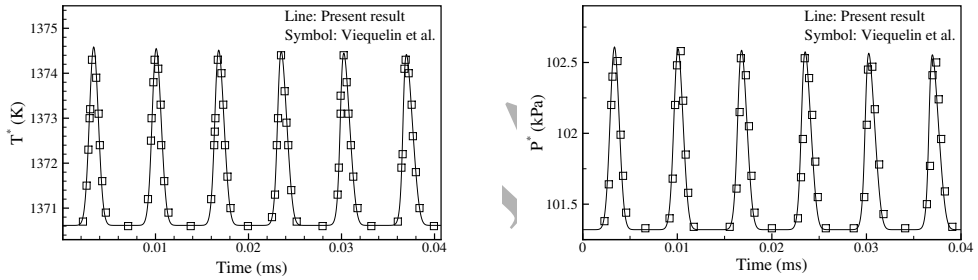

(a) Temperature (b) Pressure

Figure 1: Propagation of an acoustic wave. Time evolution of (a) temperature, (b) pressure.

In Fig. 1 we compare the results with those obtained by Vicquelin *et al.*[24] (The data are found in Ref. [16]). The results of Vicquelin *et al.* adopted here is based on the "simplified transport expressions" which is consistent with the present numerical method. From the comparison, it is found that the agreement is excellent. However, if the so called "detailed transport" method is used, the dissipation process maybe a little bit enhanced as reported in [16].

3.2. Validation of chemical modelling

The second test case focuses on the verification of the chemical production term. For this purpose, a direct way is to ignore the convective terms and to consider the pure chemical production with time. Then, the governing

equations reduce to a set of ordinary differential equations (ODE). The ODE can be solved by the Selected Asymptotic Integration Method (SAIM) as described by Weber [7].

In the first test problem, air is instantaneously heated to a temperature of 4000 K at 1.0 atm pressure. The air mixture is considered to be composed of the following five species: O_2, O, N_2, N and NO, and is assumed to be in isothermal condition. The Dunn and Kang [29] reaction mechanism is adopted for the modelling of the reactions. The time histories of the mole fractions, X_{O2} and X_O, obtained by Weber [7] and the present solver are plotted in Fig. 2(a).

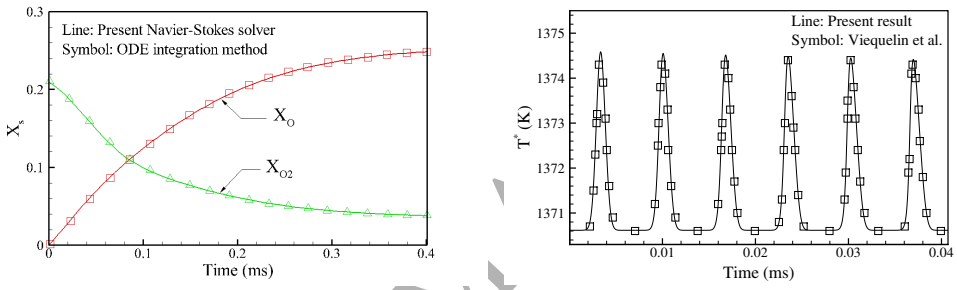

(a) Mole fraction (b) Temperature

Figure 2: Chemical modelling validation. Time evolution of (a) mole fraction of X_{O2} and X_O, (b) temperature variation with time.

The same initial conditions of $T = 4000$ K and $p = 1.0$ atm are used in the second case, but the energy absorbed and released by the reactions is taken into account, i.e., the air mixture is assumed to be in an adiabatic box. Therefore, the temperature will drop rapidly due to the dissociation reactions of oxygen and nitrogen. The temperature variation with time of the second problem is presented in Fig. 2(b).

For both cases, a good agreement is observed between the cited reference and the present numerical results, which confirms the correct implementation of the chemical reacting model of the solver. At the same time, the point-implicit scheme shows the advantage in using large time steps. For this, consider the second test problem as an example, Fig. 3 shows that the point-implicit scheme gives identical results as the time step increases from $dt = 1.0 \times 10^{-7}$ s to $dt = 1.0 \times 10^{-6}$ s, while the explicit scheme can not longer get the correct results.

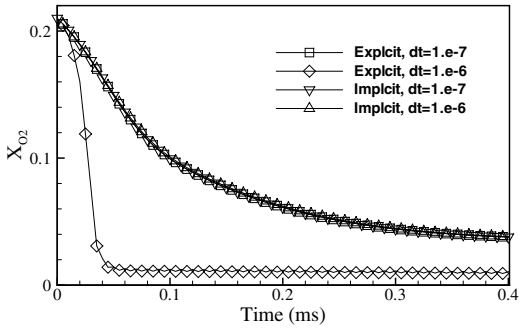

Figure 3: Comparison between point-implicit and explicit methods when time step dt increases to 1.0×10^{-6} s.

3.3. Viscous shock tube test case

The two dimensional SBLIs of a perfect gas, which were studied previously by Daru and Tenaud [15], is used as the last test case for the purpose of assessing complex flow simulations. Figure 4 shows the density field at the dimensionless time t =1, and Fig. 5 is the density distribution along the horizontal line crossing the separation bubble located at $y = 0.05$. The results for RK3-WENO5 (three stage Runge-Kutta together with fifth-order WENO scheme) on the finest grid (4000×2000) are lacking in Daru and Tenaud's paper due to prohibitively large computational time. Here we completed this simulation. The results demonstrate that the present solver is able to capture complex vortex structures and the grid converged solution is the same as that predicted by Daru and Tenaud.

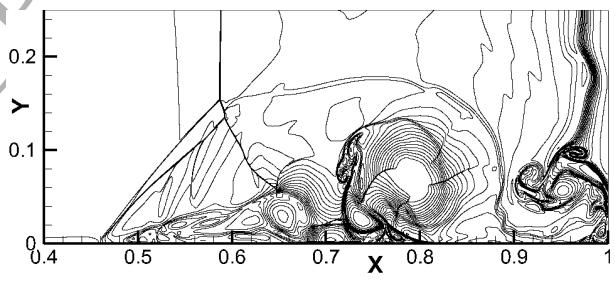

Figure 4: Density contours of present result.

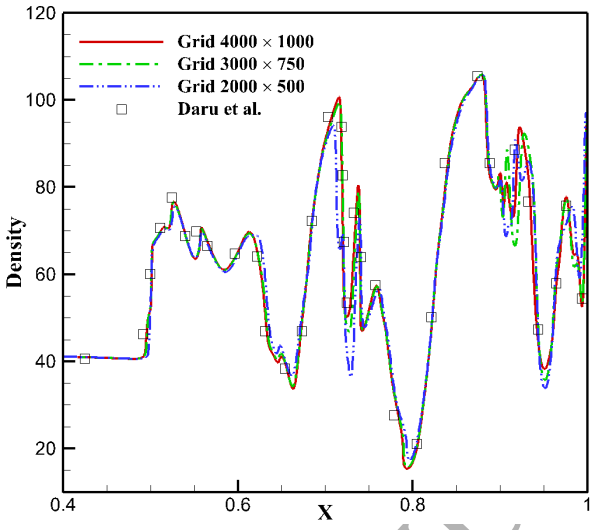

Figure 5: Comparison of density distribution along the line y=0.05.

4. Numerical simulation of the shock tube problem

4.1. Computation parameters

As main purpose of the present study, the unsteady viscous shock tube problem is studied using the developed solver. A similar two dimensional shock tube problem as designed by Daru *et al.* [15] is considered here. The computational domain consists of a two-dimensional region of 1 m length in x-direction, and 0.25 m height in y-direction. A nonreflecting boundary condition is given at the upper boundary, while no-slip adiabatic wall condition is prescribed for the other three sides. The wall is simply assumed as non-catalytic, i.e., no surface reactions take place. The diaphragm is located at the middle of the tube, and the initial states are listed in Table 1. Note that the incident shock Mach numbers are calculated by the simple shock wave theory [1], and the Reynolds numbers are estimated by the flow properties behind the incident shock.

As for the calorically perfect gas flow case, the above parameters are sufficient to define the shock tube problem. However, if real gas effects are involved, the related reference values must be specified in order to calculate the thermal and chemical properties of the flow. The reference pressure, temperature, length and velocity for the present study are set to $p_{ref} = 0.1$ Kpa, $T_{ref} = 800$ K, $L_{ref} = 1$ m, and $u_{ref} = 567$ m/s. The particular low

Table 1: Initial conditions for shock tube flow

Case	P_1	P_4	T_1	T_4	Re(cm^{-1})	Ma	Gas Model
1	1.2	120	1	1	420	2.37	Real gas
2	1.2	1200	1	1	520	3.15	Real gas
3	1.2	120	1	1	420	2.37	Calorically perfect gas
4	1.2	1200	1	1	520	3.15	Calorically perfect gas

pressure ensures a low Reynolds number, thus a good grid independence can be obtained.

The test and driver gas is standard air with 23.3% oxygen and 76.7% nitrogen in mass fraction, initially in chemical equilibrium. According to the thermo-chemical properties of air [26], for the present initial conditions the dissociation of nitrogen can be neglected. Thus, only oxygen dissociation-recombination reactions are considered in the simulation, namely,

$$O_2 + M \rightleftharpoons 2O + M,$$

where the third body M represents the three species O_2, O and N_2. The chemistry data of Park [30] is adopted to describe the chemical reactions of the air mixture.

In order to measure the dissociation level of the oxygen in the test gas, the concept of degree of dissociation is introduced here, which is defined as the fraction of dissociated atomic oxygen to the total amount of oxygen in the air mixture

$$\alpha = \frac{\rho_O}{\rho_O + \rho_{O_2}}.$$

The denominator $(\rho_O + \rho_{O_2})$ is actually a constant that is equal to the initial mass fraction of oxygen.

Some basic physical features of the shock tube flow as well as the influence of real gas effects are illustrated in Fig. 6. After the diaphragm rupture, a shock wave is generated which moves forward, followed by the contact surface. When the shock wave reaches the end-wall, it reflects and travels in the opposite direction. After shock reflection, the flow behind the reflected shock wave attain the condition of the so called "region 5" of the shock tube problem. For calorically perfect gas flow without viscosity, the corresponding parameter can be predicted by the simple shock tube theory [1], as shown by the two solid lines in the upper $x - t$ diagram of Fig. 6. However, for a real

shock tube, a boundary layer develops at the wall. The reflected shock wave interacts with the developed boundary layer, causing a interaction between shock wave and boundary layer. At the same time, high temperatures may lead to the dissociation of the test gas. In this case, there are no strict analytical solutions to describe the process. Numerical methods have to be employed to study the problem.

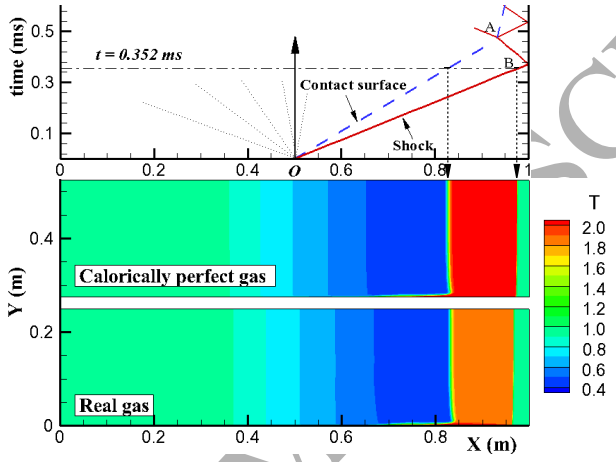

Figure 6: Comparison between numerical simulation (calorically perfect gas and real gas) and simple shock tube theory, $t = 0.352$ ms. (Case 1)

From Fig. 6, it is found that the calculated contact surface and shock front position for the calorically perfect gas model agree to the theory, except near the bottom wall, where a boundary layer develops. The dimensionless temperature behind the shock wave (denoted by T_2) is about 2.02, which is also in agreement with the theoretical value. However, for the real gas flow, the temperature T_2 decreases to about 1.82. Besides the differences of T_2, the contact surface is a little closer to the shock front for the real shock tube. This is because the density ratio across the shock front is larger when real gas effects are taken into consideration. The increased density in the flow region behind the shock shorten the distance between the shock wave and the contact surface.

4.2. Grid convergence study

After the shock wave reflection at the end wall, the flow pattern becomes quite complex. The previous study made by Sjogreen and Yee [14] has shown

that the existence of fine scale structures significantly increases the difficulty of reaching grid convergence. The simulation of viscous reacting flows is much more challenging than for non-reacting flows. Actually, strict grid independence proofs of chemically reacting flows are very rare in literature.

In the present study, test case 1 in Table 1 is chosen for the grid independence study and four grid sizes of 1000×250, 2000×500, 3000×750 and 4000×1000 cells are used. The CFL number is set to 0.2 for all cases. The grid is then split in x-direction for the parallelization. All the simulations are carried out on the "Yuan" cluster of the supercomputing center of Chinese Academy of Sciences. The calculations are ended till a dimensionless time is reached of $t = 0.57$, corresponding to the physical time t= 1 ms. The flow properties are presented in dimensionless form unless specified otherwise.

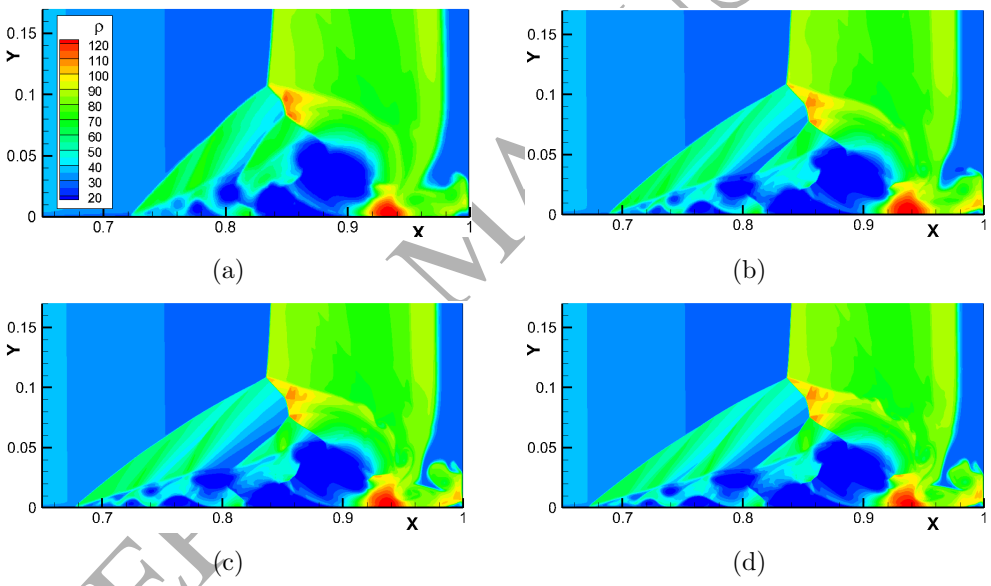

Figure 7: Grid study: density field at $t = 1$ ms, (a) 1000×250 grid points, (b) 2000×500 grid points, (c) 3000×750 grid points, (d) 4000×1000 grid points.

The comparison of the density field at $t = 1$ ms for the four grids is presented in Fig. 7. Comparing the four pictures, it is found that the density fields obtained by the four grids are basically the same. To further examine the grid independence properties, we also plot the density and the degree of dissociation along a horizontal line at $y = 0.05$, which crosses the center of the separation bubble. This can serve as a good verification of convergence. The

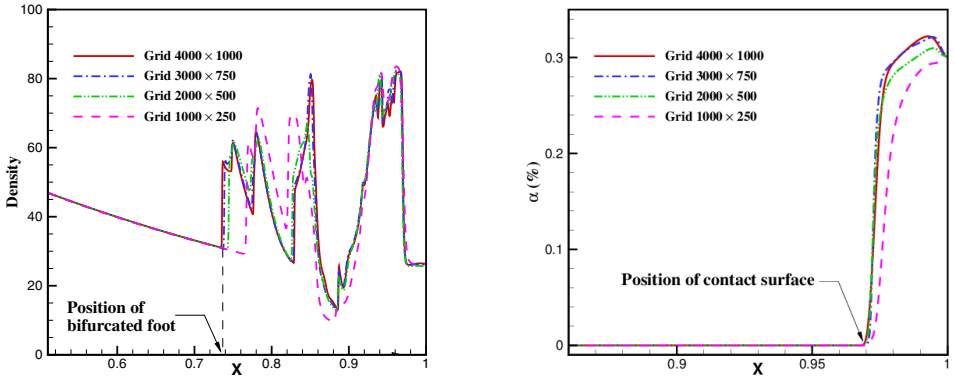

(a) (b)

Figure 8: Grid study: distribution of density (a) and degree of dissociation (b) along the line $y = 0.05$, $t = 1$ ms.

density plot indicates that the grid independent solutions are obtained for the grid 3000×750. Figure 8(b) further confirms this conclusion. Therefore, the grid with 3000×750 points is adopted for the present study.

5. Results and discussions

5.1. The SBLIs of air dissociating flow in a shock tube

A schematic picture of SBLIs is given in Fig. 9, which is firstly proposed by Mark [3] and widely accepted by the later studies. It is generally explained that the boundary layer does not have sufficient energy to penetrate the reflected shock region and begins to stagnate. At the same time, the attendant compression waves interact with the reflected shock near the wall that cause a lambda-shock structure to form [3, 7].

Fig. 10 gives the numerical temperature contours at various instants of time, which show the development of SBLIs. At time t=0.49 ms, the reflected shock wave is about 0.05 away from the end wall and is undergoing the shock/contact surface interaction. A main shock bifurcation is just visible at the bottom of the reflected shock wave, forming an early "λ" shape like shock structure. The separation bubble is seen connected to the area behind the reflected shock wave in temperature contours, which implies that it is filled with hot gas of region 5. The results indicate that the boundary layer

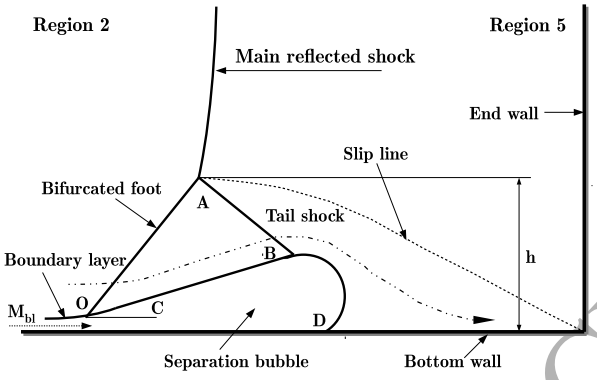

Figure 9: Schematic of shock wave and boundary layer interaction.

separates when the reverse flow injects into the incident flow. It does not stagnate to form the separation bubble, but rather goes over the bubble and enters the corner region of the shock tube. Therefore, the assumption used in Mark's [3] theory that the static pressure p_f in the region AODEB(see Fig.9) equals to the stagnation pressure in the boundary layer is not very accurate. Though this assumption is modified by a empirical relationship in Davies and Wilson's [4] model, the numerical results in present study show that the pressure distribution in this region is actually far from uniform. An appropriate averaged pressure within the separation bubble may improve the theoretical model, which is beyond the current scope.

As the flow develops, the λ-shock pattern becomes mature at time t=0.63 ms. The leading foot of the λ-shock extends into the boundary layer, and weak Mach waves are reflecting between reflected shock wave and contact surface. For the gases pass through the leading and tail foot of the λ-shock, these suffers less momentum loss than the gases decelerated by the main reflected shock. This part of high speed flow rolls up at the corner and penetrates into the bubble from the right side like a cold jet (Fig. 10(b)). The bubble starts to cool down due to the heat conduction to the cold gases around. At t=0.83 ms, a secondary bifurcation takes place at the tail foot of the λ-shock. Fig. 10(c) further tells us that the cold gases already impinged on the bottom wall and cut the bubble's connection to the hot gases. Thus, the average temperature of the separation bubble now is significantly lower than its original value.

Finally, at t=1.0 ms, the bubble extends up to the position of x=0.68,

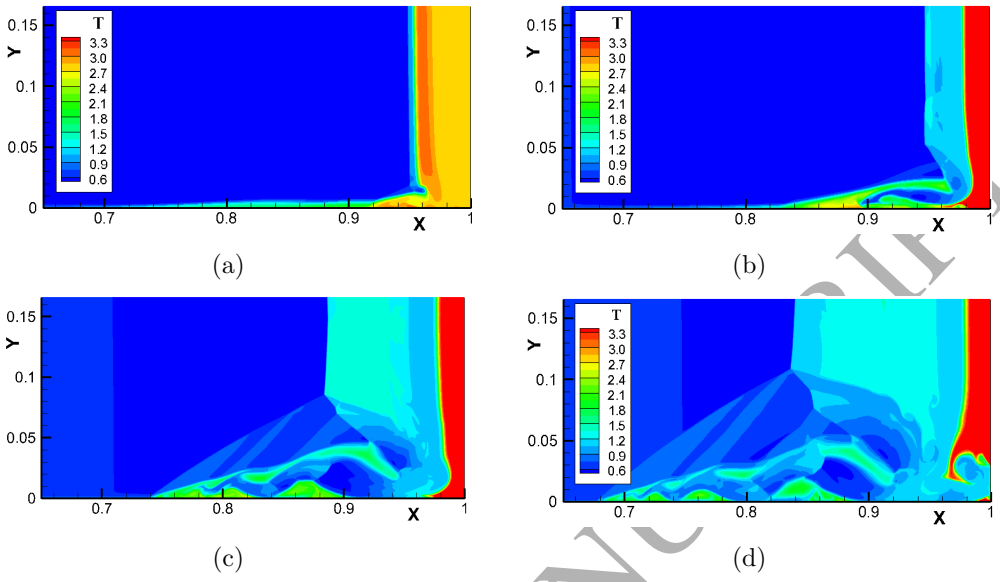

Figure 10: Computed temperature field of case 1 at time: (a) t=0.49 ms, (b) t=0.63 ms, (c) t=0.83 ms, (d) t=1.0 ms. (21 contour levels between 0.6 and 3.2)

forming a very complicated vortex structures. The secondary bifurcation on the tail foot of the λ-shock grows in size and shows the tendency to further multiple bifurcations. The typical Kelvin-Helmholtz instabilities are also observed along the slip line originating at the triple point. Temperature contours at t=1.0 ms give a more impressive image that the whole bottom part of region 5 is invaded by the cold gas, causing the so called "driver gas contamination" problem.

From Fig. 10(a) to (d), it is known that a very high temperature T_5 is established near the end wall. The associated chemical dissociations in this region as well as their effects on the SBLIs are of the interest. Fig. 11 presents the variation of the degree of dissociation for time t=0.49 ms until 1.0 ms. Since the degree of dissociation varies by several orders of magnitude, the logarithmic level labels are used in the picture. As expected, oxygen molecule dissociates in the high temperature area and the atomic oxygen concentration is built up. In Fig. 11(a), the oxygen atoms are found in the separation bubble under the foot of the λ-shock. This confirms the conclusion that the appeared bubble mostly consists of the gases coming from region 5. Comparing Fig. 11 and Fig. 10, it is found that the atomic oxygen mass fraction

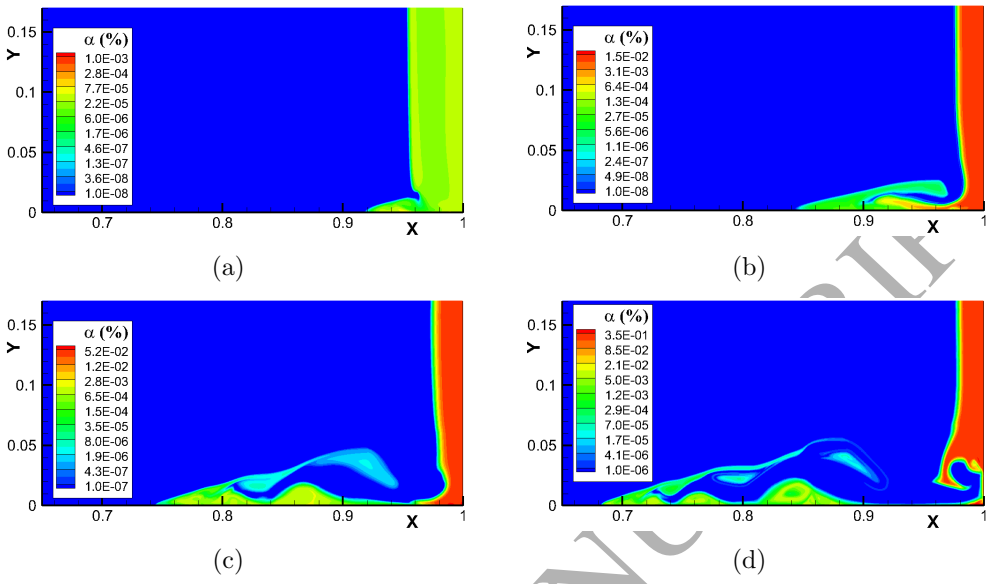

Figure 11: Computed oxygen dissociation degree for case 1 at time: (a) t=0.49 ms, (b) t=0.63 ms, (c) t=0.83 ms, (d) t=1.0 ms.

behind the reflected shock wave is mainly dependent on the temperature distribution. The similarities between the atomic oxygen mass fraction contours and temperature contours also suggest that the chemical reactions of oxygen for the condition of case 1 are actually close to the equilibrium state. This is because the majority part of the flow in region 5 is uniform and almost stationary, which allows the chemical reactions to have sufficient time to attain equilibrium. Thus, numerical simulations with chemical equilibrium model under this circumstance would not bring a significant error.

5.2. Analysis of real gas effects on SBLIs

In this section, the influence of real gas effects on SBLIs is further analyzed. When the incident shock wave is stronger, the pattern of SBLIs will exhibit some differences. The Mach number influence is studied first by comparing cases 1 and 2, as shown in Fig. 12. A general observation shows that the region near the bottom wall is a strong vorticity source due to the shear effects within the boundary layer. At about x=0.68, where the left foot of the λ-shock starts, the vortex flow divides as two parts of opposite directions, and then develops into the two largest vortical structures inside the separation bubble. At the right corner, pairing vortex filaments are created

and extend along the slip line. The vortex filaments end at locations where shock wave bifurcation occurs.

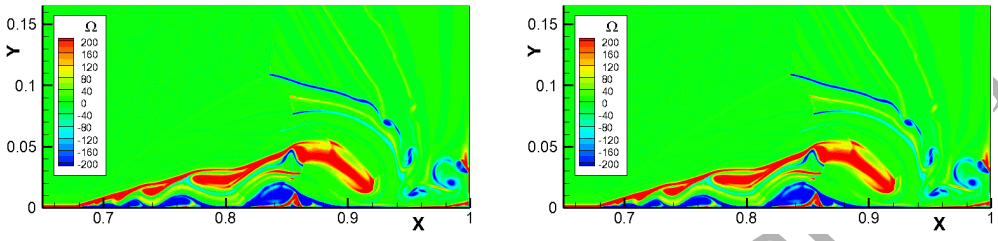

(a) (b)

Figure 12: Contours of computed vorticity field at t=1.0 ms: (a) Ma=2.37, (b) Ma=3.15. (21 contour levels between −200 and 200)

It is found that there are very regular patterns of vortices inside the separation bubble at Ma=2.37. However, as Mach number increases to 3.15, significant changes occur in the vortices field, i.e., the major pairing vortex breaks up quickly after a short distance from the head of the bifurcated shock and more complicate vortices are observed at the corner region.

Fig. 13 presents the temperature and degree of dissociation for case 2 at the dimensionless time of 1 ms. For Mach number of 3.15, the incident flow has a higher kinetic energy, and a much higher temperature is reached near the end wall after reflection. The corresponding degree of dissociation is significantly increased with a maximum value of about 75%, which means the majority part of the oxygen molecules are dissociated. Comparing Fig. 13(a) and (b), there are considerable differences between the pattern of temperature and degree of dissociation contours. These differences imply that chemical nonequilibrium effects start to play an important role for the flow of Ma=3.15.

In order to investigate the differences resulting by real gas effects of vibrational excitation and nonequilibrium dissociation, simulations with conventional calorically perfect gas model are also carried out, which are listed as case 3 and 4 in Table 1. Fig. 14 compares the temperature field of cases 2 and 4, where the upper half part is the result for air dissociating flow and the bottom part shows the result for calorically perfect gas.

Similar to what has been observed in Fig. 6, the temperature behind the reflected shock for the real gas flow is significantly lower than that of the calorically perfect gas flow. Since the pressure is insensitive to real gas

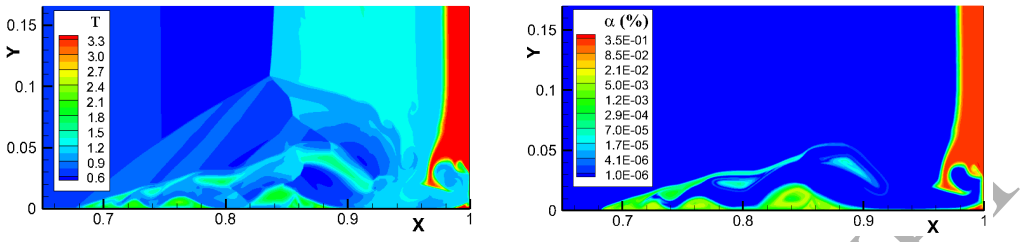

(a) (b)

Figure 13: Computed results of case 2 at t= 1 ms. (a) temperature, (b) degree of dissociation.

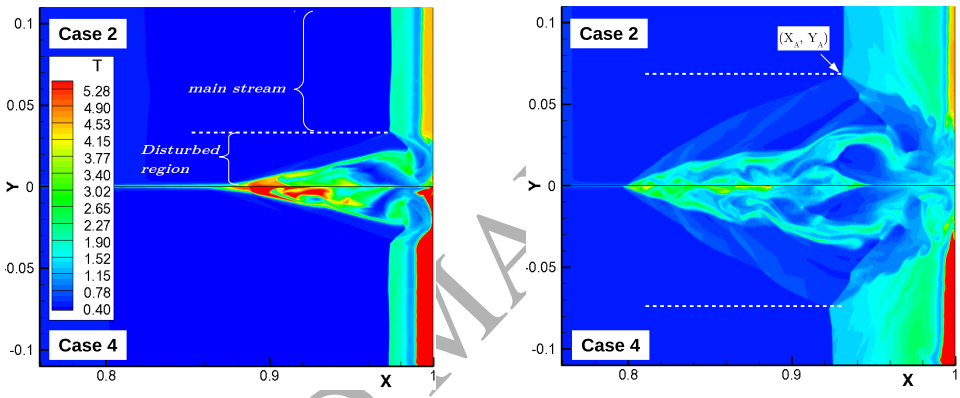

(a) t= 0.44 ms (b) t= 0.63 ms

Figure 14: Comparison between real gas and calorically perfect gas model.

effects [26], the real gas flow yields a higher density after the reflected shock wave, thus its contact surface is closer to the end wall.

As mentioned above, within simulation time(t < 1 ms), a large part of the bubble is actually composed of the reverse jet that carrying hot gas from region 5 of the shock tube flow. As the bubble moves upstream, the temperature of the bubble starts cooling down. But at a certain location, the temperature can remains very high compared to the surrounding gas. In Fig. 14(a), there is a high temperature spot at the head of the separation bubble, but it only lasts a short moment. At t = 0.63 ms, as displayed in Fig. 14(b), the temperature in the separation bubble is much lower than in region 5. Though the high temperature spot is not sustainable, the temperature within the separation bubble is still worth for paying attention since it may

become a potential ignition spot if a combustible gas is presented in the shock tube.

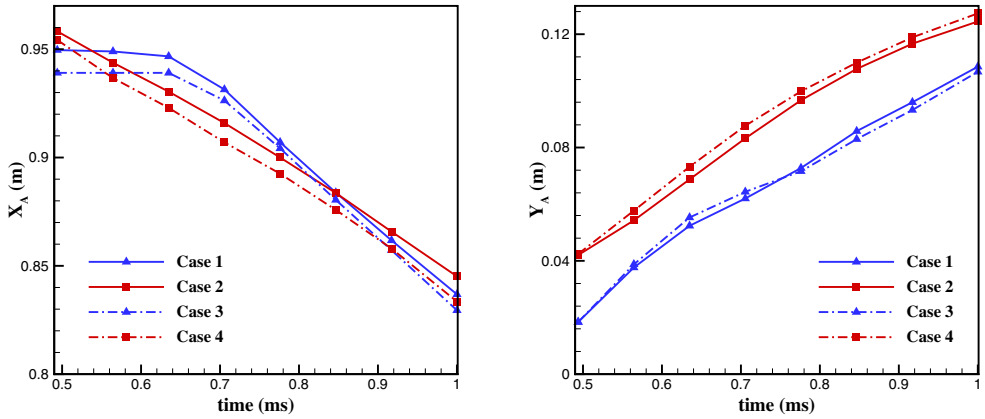

(a) x coordinate (b) y coordinate

Figure 15: Triple point position $A(X_A, Y_A)$ versus time.

The white dashed lines in Fig. 14 divide the flow into the main stream area and the disturbed region at the triple point $A(X_A, Y_A)$. To make a close scrutiny about the variation of the triple point trajectory, Fig. 15 shows the time evolution of the triple point position. The dash-dotted line and the solid line denote the results obtained by the calorically perfect gas and real gas model, respectively. The slope of the lines represents the x- and y-velocity of the triple point. It is found that the results of cases 1 and 3 are very close to each other, indicating that the triple point position is barely affected by real gas effects at Ma=2.37. As Mach number increases to 3.15, it is clear that case 2 has a higher X_A-value and a lower Y_A-value compared to case 4. The higher X_A-value means the λ-shock in real gas flow moves slower, which can be attributed to the considerable energy consumption by the air dissociation reactions and thus the shock wave becomes less energetic. In contrast, the lower Y_A-value indicates that the disturbed region is smaller in real gas flow. This phenomenon is expected since the density within the λ-shock will increase when the real gas effects are involved.

In addition, Fig. 15(b) shows that the Y_A-value for Ma=3.15 (cases 2 and 4) is much larger than that of Ma=2.37 (cases 1 and 3), which suggests that

the size of the disturbed region will significantly increase as Mach number increases. For the cases 1 and 3 in Fig. 15(a) , the triple point shows little changes in x-direction for times less than about 0.63 ms. The formed λ-shock seems to stop moving to the left while only increasing its size in the y-direction, which implies that the leading shock angle increases significantly at this stage. The time period corresponding to the shock/contact-surface interaction as displayed in Fig. 10 (a) to (b), and this interaction causes the reflected shock to stop for a very short moment.

6. Concluding remarks

A high-order point-implicit solver has been developed for the multicomponent chemically reacting flows, and is applied to study the shock wave/boundary-layer interactions (SBLIs) of an air dissociating flow in a shock tube. For a low shock Mach number case of 2.37, regular vortex arrangements are observed in the flow field and the gas flow is close to chemical equilibrium. When Mach number increases to 3.15, the vortex structures break up, leading to very complicated flow pattern, and the air dissociation reactions are far from equilibrium. By comparing the triple point trajectory of SBLIs, it is found that the λ-shock in real gas flow moves slower and has a smaller disturbed region than in the perfect gas flow. The study demonstrates the solver's ability in the simulation of complex chemical reacting flow and also sheds some lights on the interaction process between shock wave and boundary layer in a shock tube.

To further study the related phenomena of SBLIs, such as transition to turbulence, corner effects etc., the complete three-dimensional simulation is needed. Though it is possible, the computational cost is prohibitive for the present study. However, it is quite interesting and promising to conduct these simulations in the near future.

Acknowledgements

The present numerical solver was developed at the Shock Wave Laboratory of RWTH Aachen University, under the CAS-DAAD Joint Fellowship Programme for Doctoral Students of CAS. The authors acknowledge the Chinese Academy of Sciences and the German Academic Exchange Service for providing the financial support.

Appendix A. Eigenvectors for multispecies flow

In present study, the Jacobi matrices are derived as

$$A = \frac{\partial F}{\partial U} = \begin{bmatrix} u(\delta_{ij} - Y_i) & Y_i & 0 & 0 \\ \beta_j - u^2 & -\beta u + 2u & -\beta v & \beta \\ -uv & v & u & 0 \\ \beta_j u - uh & -\beta u^2 + h & -\beta uv & \beta u + u \end{bmatrix},$$

$$B = \frac{\partial G}{\partial U} = \begin{bmatrix} v(\delta_{ij} - Y_i) & 0 & Y_i & 0 \\ -uv & v & u & 0 \\ \beta_j - v^2 & -\beta u & -\beta v + 2v & \beta \\ \beta_j v - vh & -\beta uv & -\beta v^2 + h & \beta v + v \end{bmatrix},$$

where h is the dimensionless total enthalpy of the gas mixture

$$h = e_t + \frac{1}{\gamma_r \mathbf{M}_r^2} \frac{p}{\rho}.$$

And β, β_j are pressure partial derivatives, which will be specified later. δ_{ij} is Kronecker-Delta. The eigenvalues are

$$\lambda_1^F = \lambda_2^F = ... = \lambda_{N+1}^F = u, \quad \lambda_{N+2}^F = u + c, \quad \lambda_{N+3}^F = u - c,$$

$$\lambda_1^G = \lambda_2^G = ... = \lambda_{N+1}^G = v, \quad \lambda_{N+2}^G = v + c, \quad \lambda_{N+3}^G = v - c,$$

where the dimensionless frozen sound of speed is defined as

$$c = \sqrt{\frac{1}{\gamma_r \mathbf{M}_r^2}(1 + \beta)\frac{p}{\rho}}.$$

The right eigenvectors are solved from the algebraic equations $A\mathbf{R}_i = \lambda_i \mathbf{R}_i$ and the left eigenvectors are obtained by solving the algebraic equations $\mathbf{RL} = \mathbf{I}$ (or $\mathbf{LR} = \mathbf{I}$). The final expressions are

$$R^F = \begin{bmatrix} \delta_{ij}/c^2 & 0 & Y_s/2c^2 & Y_s/2c^2 \\ u/c^2 & 0 & (u + c)/2c^2 & (u - c)/2c^2 \\ v/c^2 & 1 & v/2c^2 & v/2c^2 \\ [\beta(u^2 + v^2) - \beta_j]/\beta c^2 & v & (h + uc)/2c^2 & (h - uc)/2c^2 \end{bmatrix},$$

$$L^F = \begin{bmatrix} c^2\delta_{ij} - Y_i\beta_j & \beta u Y_i & \beta v Y_i & -\beta Y_i \\ -v & 0 & 1 & 0 \\ \beta_j - uc & c - \beta u & -\beta v & \beta \\ \beta_j + uc & -c - \beta u & -\beta v & \beta \end{bmatrix},$$

$$R^G = \begin{bmatrix} \delta_{ij}/c^2 & 0 & Y_i/2c^2 & Y_i/2c^2 \\ u/c^2 & 1 & u/2c^2 & u/2c^2 \\ v/c^2 & 0 & (v+c)/2c^2 & (v-c)/2c^2 \\ [\beta(u^2+v^2) - \beta_j]/\beta c^2 & u & (h+vc)/2c^2 & (h-vc)/2c^2 \end{bmatrix},$$

$$L^G = \begin{bmatrix} c^2\delta_{ij} - Y_i\beta_j & \beta u Y_i & \beta v Y_i & -\beta Y_i \\ -u & 1 & 0 & 0 \\ \beta_j - vc & c - \beta u & -\beta v & \beta \\ \beta_j + vc & -c - \beta u & -\beta v & \beta \end{bmatrix}.$$

It should be mentioned that the geometric coefficients are also involved in the eigenvectors if transformed coordinates are used. The expressions of the β, β_j are briefly derived as follow.

Firstly, the derivative of the total energy can be written as

$$\begin{aligned} d(\rho e_t) = d\left[\rho\frac{u^2+v^2}{2} + \rho e\right] &= ud(\rho u) - \frac{1}{2}u^2\sum_{j=1}^{N} d\rho_j + vd(\rho v) \\ &- \frac{1}{2}v^2\sum_{j=1}^{N} d\rho_j + \rho c_v dT + \sum_{j=1}^{N} e_j d\rho_j. \end{aligned} \tag{A.1}$$

Solving the temperature from the above expression, gives

$$dT = \frac{1}{\rho c_v}\left[d(\rho e_t) - ud(\rho u) - vd(\rho v) + \sum_{j=1}^{N}\frac{u^2+v^2}{2} - \beta e_j\right]. \tag{A.2}$$

The pressure for a multispecies flow is a function of temperature and species density, $p = p(T, \rho_1, \ldots, \rho_N)$. Therefore, the pressure derivative is

$$dp = \rho R dT + T\sum_{j=1}^{N} R_s d\rho_j. \tag{A.3}$$

Then, substitute dT into dp, we get the pressure derivative with respect to conserved variables

$$dp = \beta d(\rho e_t) - \beta u d(\rho u) - \beta v d(\rho v) + \sum_{j=1}^{N} (\beta \frac{u^2+v^2}{2} - \beta e_s + TR_s) d\rho_j. \tag{A.4}$$

where $\beta = R/c_v$, and for perfect gas $\beta = \gamma - 1$. The expressions for the pressure partial derivatives in eigenvectors are

$$\beta = \frac{\partial p}{\partial(\rho e_t)} = \frac{R}{c_v}, \quad \beta_j = \frac{\partial p}{\partial j} = \beta \frac{u^2+v^2}{2} - \beta e_j + TR_j. \tag{A.5}$$

The other pressure partial derivatives are

$$\frac{\partial p}{\partial(\rho u)} = -\beta u, \quad \frac{\partial p}{\partial(\rho v)} = -\beta v. \tag{A.6}$$

Appendix B. Source term Jacobian

For the implicit treatment of the chemical source term, the evaluation of the Jacobian $\partial S/\partial U$ is required for each grid point. Substitution of $\dot{\omega}_i$ into $\partial S/\partial U$ yields

$$\frac{\partial \dot{\omega}_i}{\partial U_j} = M_i \sum_{r=1}^{nr} \left\{ (v_{i,r}^{"} - v_{i,r}^{'}) \cdot (q_{f,r} - q_{b,r}) \right\},$$

where

$$q_{f,r} = k_{f,r} \left[\left(\frac{\alpha_{f,r}}{T} + \frac{E_{f,r}}{T^2} \right) \frac{\partial T}{\partial U_j} + \frac{v_{j,r}^{'}}{\rho_j} \right] \prod_{s=1}^{N} (\frac{\rho_s}{Ms})^{v_{s,r}^{'}},$$

$$q_{b,r} = k_{b,r} \left[\left(\frac{\alpha_{b,r}}{T} + \frac{E_{b,r}}{T^2} \right) \frac{\partial T}{\partial U_j} + \frac{v_{j,r}^{"}}{\rho_j} \right] \prod_{s=1}^{N} (\frac{\rho_s}{Ms})^{v_{s,r}^{"}},$$

Thus, the calculation of the source term Jacobian is reduced to solve the temperature derivatives with conservative variables, which are

$$\frac{\partial T}{\partial \rho u} = -\frac{u}{\rho c_v}, \quad \frac{\partial T}{\partial \rho v} = -\frac{v}{\rho c_v},$$
$$\frac{\partial T}{\partial \rho E} = \frac{1}{\rho c_v}, \quad \frac{\partial T}{\partial \rho_j} = \frac{1}{\rho c_v} \left(\frac{u^2+v^2}{2} - \beta e_j \right).$$

References

[1] A.G. Gaydon. *The shock tube in high-temperature chemical physics*. CHAPMAN and HALL LTD., London, 1963.

[2] R.J. Stalker and K.C.A. Crane. Driver gas contamination in high-enthalpy reflected shock tunnel. *AIAA Technical notes*, pages 277–279, 1977.

[3] H. Mark. The interaction of a reflected shock wave with the boundary layer in a shock tube. Technical Report Technical memorandum 1318, NASA, 1958.

[4] L. Davies and J. Wilson. Influence of reflected shock and boundary-layer interaction on shock-tube flows. *Phys. Fluids*, supplement 1:37–43, 1969.

[5] K. Matsuo, S. Kawagoe, and K. Kage. The interaction of a reflected shock wave with the boundary layer in a shock tube. *Bull ASME*, 17(110):1039–46, 1969.

[6] Y.S. Weber, J.P. Boris, and J.D. Anderson. The numerical simulation of shock bifurcation near the end wall of a shock tube. *Phys. Fluids*, 7(10):2475–2488, 1995.

[7] Y.S. Weber. *The numerical simulation of the reflected-shock/boundary-layer interaction in shock tubes*. PhD thesis, University of the Maryland College Park, 1994.

[8] V. Daru and C. Tenaud. Evaluation of TVD high resolution schemes for unsteady viscous shocked flows. *Comput. Fluids*, 30:89–113, 2001.

[9] M. Lamnaouer, A.J. Kassab, E. Divo, R. G. Urquiza, Polley N. L., and E. L. Petersen. Time-accurate simulation of shock propagation and reflection in an axi-symmetric shock tube. *AIAA 2010-926*, 2010.

[10] H. Chen, C. Wen, and Yang C. Numerical simulation of the Air-He shock tube flow with equilibrium air model. *AIAA Journal*, 50(9):1817–1825, 2012.

[11] I. Matthias, S. Yong, and D. Ralf. Detailed simulations of shock-bifurcation and ignition of an argon-diluted hydrogen/oxygen mixture in a shock tube. *AIAA 2013-0538*, 2013.

[12] B. Xiong, X. Fan, Y. Wang, L. Zhou, and Y. Tao. Back-pressure effects on unsteadiness of separation shock in a rectangular duct at Mach 3. *Acta Astronaut.*, 141:248–254, 2017.

[13] A.A. Pasha, K. A. Juhany, and M. Khalid. Numerical prediction of shock/boundary-layer interactions at high Mach numbers using a modified Spalart-Allmaras model. *Eng. Appl. Comp. Fluid*, 12:459–472, 2018.

[14] B. Sjogreen and H.C. Yee. Grid convergence of high order methods for multiscale complex unsteady viscous compressible flows. *J. Comput. Phys*, 185:1–26, 2003.

[15] V. Daru and C. Tenaud. Numerical simulation of the viscous shock tube problem by using a high resolution monotonicity-preserving scheme. *Comput. Fluids*, 38:664–675, 2009.

[16] Pefro J.M. Ferrer, R. Buttay, G. Lehnasch, and A. Mura. A detailed verification procedure for compressible reactive multicomponent Navier–Stokes solvers. *Comput. Fluids*, 89:88–110, 2014.

[17] A. Ern. Fast and accurate multicomponent transport property evaluation. *J. Comput. Phys*, 120:105–116, 1995.

[18] A. Ern and V. Giovangigli. Thermal diffusion effects in hydrogen-air and methane-air flames. *Combust. Theor. Model.*, 2:349–372, 1998.

[19] S. Chen and Q. Sun. Numerical study of shock/boundary layer interaction of chemically reacting flow in shock tube. *Procedia Eng.*, 126:617–621, 2015.

[20] S. Chen, Y. Hu, and Q. Sun. Study of the coupling between real gas effects and rarefied effects on hypersonic aerodynamics. In *AIP Conference Proceedings*, volume 1501, pages 1515–1521, 2012.

[21] S. Chen and Q. Sun. A quasi-one-dimensional model for hypersonic reactive flow along the stagnation streamline. *Chinese J. Aeronaut.*, 29(6):1517–1526, 2016.

[22] Y. Yao, L. Krishnan, and G.T. Roberts. The effect of Mach number on unstable disturbances in shock/boundary-layer interactions. *Phys. Fluids*, 19(054104):1–15, 2007.

[23] V. Moureau, G. Lartigue, Y. Sommerer, C. Angelberger, O. Colin, and T. Poinsot. Numerical methods for unsteady compressible multi-component reacting flows on fixed and moving grids. *J. Comp. Phys.*, 202:710–736, 2005.

[24] R. Vicquelin, B. Fiorina, S. Payet, N. Darabiha, and O. Gicquel. Coupling tabulated chemistry with compressible CFD solvers. *Proc. Combust. Inst.*, 33:1481–1488, 2011.

[25] G. Ribert, O. Gicquel, N. Darabiha, and D. Veynante. Tabulation of complex chemistry based on self-similar behavior of laminar premixed flames. *Combust. Flame*, 146:649–664, 2006.

[26] J.D. Anderson. *Hypersonic and high-temperature gas dynamic*. McGraw-Hill, 1989.

[27] J.M. Bonnie, J.Z. Michael, and G. Sanford. NASA glenn coefficients for calculating thermodynamic properties of individual species. Technical Report TP–2002–211556, NASA, 2000.

[28] C.R. Wilke. A viscosity equation for gas mixtures. *J. Chem. Phys*, 18:517–519, 1950.

[29] M.G. Dunn and S. Kang. Theoretical and experimental studies of reentry plasmas. Technical Report NASA-CR-2232, NASA, 1973.

[30] C. Park. An assessment of two-temperature kinetic model for ionizing air. *AIAA-87-1574*, 1987.

[31] G.S. Jiang and C.W. Shu. Efficient implementation of weighted ENO schemes. *J. Comput. Phys*, 126:202–28, 1996.

[32] I. Klioutchnikov and H. Olivier. A numerical study of pressure/shock waves interactions in transonic airfoil flow using optimized WENO schemes. *AIAA 2010-924*, 2010.

[33] A. Graf and U. Riedel. Numerical simulation of supersonic reactive flows using explicit Runge-Kutta methods. *AIAA 2000-438*, 2000.

[34] F. Togashi, U. R. Lohner, and N. Tsuboi. Numerical simulation of H2/Air detonation using detailed reaction models. *AIAA 2006-954*, 2006.

[35] I. Klioutchnikov, H. Olivier, and J. Odenthal. Numerical investigation of coaxial jets entering into a hot environment. *Comput. Fluids*, 86:490–499, 2013.